Journal of Inorganic Biochemistry 283 (2026) 113367

Contents lists available at ScienceDirect

Journal of Inorganic Biochemistry

journal homepage: www.elsevier.com/locate/jinorgbio

Synthesis, characterization, Hirshfeld surface analysis of V-substituted Keggin polyoxotungstates and Ca^{2+}-ATPase inhibiting potential

Islem Meskini [a,*], Gil Fraqueza [b,d], Frédéric Capet [c], Manuel Aureliano [d,e,*], Brahim Ayed [a,*]

[a] Laboratory of Physico-Chemistry of Materials LR01ES19, Faculty of Sciences, University of Monastir, Monastir 5019, Tunisia
[b] Instituto Superior de Engenharia, Universidade do Algarve, 8005-139 Faro, Portugal
[c] Université Lille, CNRS, Centrale Lille, ENSCL, Université Artois, Unité de Catalyse et Chimie du Solide, F-59000 Lille, France
[d] Centro de Ciências do Mar do Algarve (CCMAR/CIMAR LA), Universidade do Algarve, Campus de Gambelas, 8005-139 Faro, Portugal
[e] Faculdade de Ciências e Tecnologia (FCT), Universidade do Algarve, Campus de Gambelas, 8005-139 Faro, Portugal

ARTICLE INFO

Keywords:
Vanadium substituted Keggin polyoxometalates
Hybrid polyoxometalates
Calcium ATPase inhibition
Polyoxometalate synthesis
Enzyme coupled assay
Hirshfeld surface analysis

ABSTRACT

Polyoxometalates (POMs) biological and biomedical applications have attracted increasing attention over the past decades. Polyoxometalates are inorganic transition metal oxygen clusters characterized by having multiple structures and tunable electronic properties that are well-known to be effective inhibitors of many enzymes, such as ATPases. Herein, a new hybrid POM of the Keggin type, Vanadium-substituted Keggin polyoxotungstate, namely $(C_6H_{15}N)_4(C_6H_{16}N)_6(VW_{12}O_{40})_2{\cdot}4H_2O$, was synthesized via wet-chemical methods in aqueous solution. Its purity was confirmed, and the compound was fully characterized by single-crystal X-ray diffraction, infrared spectroscopy, UV–visible spectroscopy, and thermogravimetric analysis. The Keggin-type compound exhibited a half maximal inhibitory concentration (IC_{50}) value of 8.25 μM toward calcium adenosine triphosphatase (Ca^{2+}-ATPase) inhibition, as measured spectrophotometrically using a coupled pyruvate kinase/lactate dehydrogenase enzyme assay. Hirshfeld surface analysis was employed to investigate intermolecular interactions within the crystal structure, revealing differences in hydrogen bonding and oxygen-based contacts. These structural features may suggest a possible relationship with the observed biological activity; however, no direct correlation with Ca^{2+}-ATPase inhibition can be firmly established from the present data. Therefore, the observed relationships should be considered preliminary and structural in nature, rather than mechanistic. Further computational and biological studies are required to clarify the role of these interactions in enzyme inhibition.

1. Introduction

A literature search conducted on Web of Science in January 5, 2026 revealed more than 8000 published articles about polyoxometalates (POMs), approximately 87% (7000) related to the keyword “chemistry” (being 2642 for “synthesis” and 1806 for “catalysis), whereas for “environment”, and “medicine” a total of about 900 (11%) and 400 (5%) articles were found, respectively. For “polyoxometalates” combine with “proteins” it was found only 244 published papers and combine with MOFs (metal organic frameworks) already 229 papers, the chemistry Nobel Prize 2025. Still, the applications of POMs in environmental science and/or medicine are growing in the last decades. In fact, POMs relationship to sustainable development and green chemistry is clearly increasing, for example, in the degradation of water emerging pollutants such as dyes, microplastics, and antibiotics, in addition to well-known organic and inorganic contaminants [1–6]. Moreover, at the 21 century, POMs are also recognized as novel antibacterial agents for fighting against bacterial resistance and by showing promissory effects in the treatment of several types of cancer as well as in specific neurological diseases such as in Alzheimer diseases [7–13].

Abbreviations: A23187, Calcium ionophore; BSA, Bovine serum albumin; CE, Celecoxib; CPA, Cyclopiazonic Acid; *E*-NTPDase, Ecto-Nucleoside Triphosphate Diphosphohydrolases; HEPES, 4-(2-hydroxyethyl)-1-piperazineethanesulfonic acid; HSA, Human serum albumin; IC_{50}, Concentration that induces 50% of inhibition of the enzymatic activity; LDH, Lactate Dehydrogenase; NADH, Nicotinamide Adenine Dinucleotide; PEP, Phosphoenolpyruvate; PK, Pyruvate Kinase; POM-1, $(C_6H_{15}N)_4(C_6H_{16}N)_6(VW_{12}O_{40})_2{\cdot}4(H_2O)$; POM-2, $(C_7H_{11}N_2)_4(V_{2.21}W_{3.79}O_{19}){\cdot}4(H_2O)$; POM-3, $(C_2H_8N)_6(V_2Mo_{18}O_{62}){\cdot}3(H_2O)$; POM-4, $(C_4H_{16}N_3)_4(V_2W_4O_{19})_3{\cdot}12(H_2O)$; POMos, Polyoxomolybdates; POMs, Polyoxometalates; POTs, Polyoxotungstates; POVs, Polyoxovanadates; SRVs, Sarcoplasmic reticulum vesicles; TG, Thapsigargin.

* Corresponding authors.
E-mail addresses: a91160@ualg.pt (I. Meskini), maalves@ualg.pt (M. Aureliano), ayedbrahim@yahoo.com (B. Ayed).

https://doi.org/10.1016/j.jinorgbio.2026.113367
Received 29 January 2026; Received in revised form 13 May 2026; Accepted 29 May 2026
Available online 1 June 2026
0162-0134/© 2026 The Authors. Published by Elsevier Inc. This is an open access article under the CC BY license (http://creativecommons.org/licenses/by/4.0/).

Although the molecular mechanisms of action in biologic systems are yet to be clearly understood, POMs effects might be due, at least in part, to its specific interactions with biomolecules such as proteins, thus affecting (stimulating or inhibiting) several physiological and pathological processes [14–16]. Aureliano's group, in conjunction with other groups and collaborators, extensively studied the interactions of POMs with proteins, particularly decavanadate (V_{10}) [16–20] and recently polyoxotungstates (POTs) [14,15]. In several cases these POM–protein interactions, are mainly of electrostatic nature being the negatively charged metal clusters found within positively charged regions of proteins, although others modes of interaction might also occur [16–18].

POMs can exhibit diverse structures (Keggin, Dawson, Lindqvist) and possess high thermal stability, redox versatility, and tunable acidity, making them valuable in chemistry, environment and medicine [1,3,6–13,15–17,19,20]. Hybrid POMs, formed by covalently or non-covalently attaching organic ligands to POMs, combine the intrinsic properties of POMs with enhanced solubility, stability, and tunable interactions. Hybrid POMs are widely studied for a broad range of applications, including environmental remediation (such as the removal of emerging pollutants) [21], health related issues (including diabetes, Alzheimer's disease, and cancer) [13], as well as in sensing [22], catalysis [23], materials science [24], and molecular electronics [25]. Their structural versatility and tunable properties make them particularly attractive for designing functional materials with tailored chemical and biological activities [26].

Classical POMs primarily interact with proteins through non-covalent forces, including electrostatic attractions, hydrogen bonding, and van der Waals interactions, which govern their reversible and selective binding. In contrast, hybrid POMs, functionalized with organic ligands, introduce additional hydrophobic regions, steric effects, and enhanced hydrogen-bonding capabilities. These modifications enable more precise molecular recognition, higher binding affinity, and tunable biological activity. As a result, hybrid POMs are particularly promising for a range of biological interactions, including: interaction with Ca^{2+}-ATPase [27], binding to serum albumins (BSA/HSA) [28], inhibition of phosphatases and kinases [29], binding to DNA double helices [30], interaction with RNA and ribonucleoprotein complexes [31], modulation of amyloid protein aggregation [32], and interaction with redox-active enzymes [33].

Hirshfeld surface analysis provides a powerful visual and quantitative tool to explore and quantify intermolecular interactions in crystalline materials, including hydrogen bonds, van der Waals contacts, and π–π stacking. By mapping electron density and contact distances, this approach allows a comprehensive understanding of molecular packing, non-covalent interactions, and ligand coordination [34]. It is particularly valuable for studying POMs and hybrid POMs, as it reveals subtle features of their binding modes, supramolecular arrangements, and interactions with biomolecules, which are critical for rational design of functional materials, catalysts, and bioactive compounds [35]. However, Hirshfeld surface analysis is limited to the solid-state structure and does not directly provide information on interactions with biomolecules or enzymatic binding mechanisms. Nevertheless, it can contribute to the structural characterization of materials that may be relevant for crystal engineering and the design of functional inorganic systems [36].

Based on the overall aim of the study, it seeks to investigate the relationship between structural features and Ca^{2+}-ATPase inhibiting potential of vanadium-substituted Keggin polyoxotungstates by integrating physicochemical, crystallographic, and supramolecular analyses, in order to better understand the factors influencing their Ca^{2+}-ATPase inhibitory activity and to support the rational design of future effective inhibitors. The specific aims of this study are: i) synthesis of V-substituted Keggin polyoxotungstates, $(C_6H_{15}N)_4(C_6H_{16}N)_6(VW_{12}O_{40})_2{\cdot}4H_2O$ (abbreviated $VW_{12}O_{40}$) ii) characterization of V-substituted Keggin polyoxotungstates by infrared spectroscopy, UV–visible spectroscopy, thermogravimetric analysis, and single-crystal X-ray diffraction; iii) Hirshfeld surface analysis comparative study of Keggin $VW_{12}O_{40}$ with one Dawson and two hybrid Lindqvist POTs; iv) evaluation of the $VW_{12}O_{40}$ inhibition potential regarding Ca^{2+}-ATPase activity; v) analysis of possible correlations between Hirshfeld surface parameters and Ca^{2+}-ATPase inhibitory activity of $VW_{12}O_{40}$, one Dawson, and two hybrid Lindqvist POTs; vi) Analysis of recent literature correlations between POMs electronic properties with biological activities.

2. Materials and methods

2.1. Reagents

Sodium tungstate dihydrate ($Na_2WO_4{\cdot}2H_2O$), vanadium oxide (V_2O_5), triethylamine ($C_6H_{15}N$), hydrochloric acid, potassium chloride (KCl), HEPES, sucrose, magnesium chloride ($MgCl_2$), calcium chloride ($CaCl_2$), phosphoenolpyruvate (PEP), adenosine triphosphate (ATP), nicotinamide adenine dinucleotide (NADH), lactate dehydrogenase, pyruvate kinase, and ionophore A23187 (calcimycin) were purchased from Sigma-Aldrich or Merck (Darmstadt, Germany) and used as received.

2.2. Characterization

Single-crystal X-ray diffraction data for the hybrid polyoxometalate were collected at 107 K using a Bruker PHOTON III DUO diffractometer equipped with a microfocus sealed X-ray tube. Preliminary diffraction images indicated a triclinic system and suggested the $P1^{-}$ space group. The crystal structure was solved by direct methods using the SHELXS-2019 [37] program, which allowed the identification of both inorganic and organic fragments. The remaining non-hydrogen atoms were located from successive difference Fourier maps and refined using SHELXL-2019 [38]. In the final full-matrix least-squares refinement, hydrogen atoms were included in calculated positions and refined with isotropic displacement parameters. The refinement converged with Rint = 0.048. Crystallographic data and refinement details are summarized in Table S1. Additional crystallographic information for this compound has been deposited at the Cambridge Crystallographic Data Centre (CCDC) under the deposition number CCDC 2522903. Functional groups were identified by Fourier-transform infrared (FT-IR) spectroscopy at room temperature using a Spectrum BX II PerkinElmer spectrometer in the range of 400–4000 cm^{-1}. The optical properties of the compound were investigated by UV–visible spectroscopy in the 200–900 nm range using a SECOMAM spectrophotometer, with the sample dissolved in deionized water. Elemental analyses (C, H, and N) were performed using a Vario EL III elemental analyzer. Thermogravimetric analysis was carried out on a Netzsch STA 449 F3 Jupiter thermal analyzer under a nitrogen atmosphere at a heating rate of 10 °C·min^{-1}.

2.3. Preparation of sarcoplasmic reticulum vesicles and POMs solutions

Sarcoplasmic reticulum vesicles (SRV) enriched in Ca^{2+}-ATPase were prepared from rabbit skeletal muscle according to previously published procedures [14,27,39,40]. The vesicles were suspended in a solution containing 0.1 M KCl and 10 mM HEPES (pH 7.0), mixed in equal volume with 2.0 M sucrose, then rapidly frozen in liquid nitrogen and stored at −80 °C. SDS-PAGE analyses confirmed that Ca^{2+}-ATPase represented at least 70% of the total protein content, in agreement with earlier reports [40]. Stock solutions of the POM compounds (1 mM) were freshly prepared by dissolving the solid material in Milli-Q water and maintaining the solutions at room temperature until use.

2.4. Determination of Ca^{2+}-ATPase IC_{50}values

For carrying out the determination of Ca^{2+}-ATPase activity assays, the following medium was prepared: 25 mM HEPES (pH 7.0), 100 mM KCl, 5 mM $MgCl_2$ and 50 μM $CaCl_2$. The experiments were performed with isolated sarcoplasmic reticulum vesicles (SRVs) previously diluted

to 1 mg/ml with a sucrose concentration of 0.25 M. To 0.8 mL of medium described above, it was added, into a quartz cuvette, 0.42 mM phosphoenolpyruvate (PEP), 18 IU lactate dehydrogenase (LDH), 7.5 IU 155 pyruvate kinase (PK), and 2.5 mM ATP without (control) or with increasing concentrations of $VW_{12}O_{40}$ (from 2.5 to 20 μM) were added to this medium. POMs were added after addition of the medium and before the addition of the enzymes of the coupled assay (lactate dehydrogenase (LDH) and pyruvate kinase (PK)). The absorbance of the solution was measured spectrophotometrically at 340 nm, at 25 °C, and an auto zero was performed. Subsequently, 0.25 mM NADH (nicotinamide adenine dinucleotide) was added, allowing the absorbance value to stabilize to about 1.3 O.D. (optical density). The assay begins after the addition of 10 μg/mL of Ca^{2+}-ATPase (basal activity) and one minute after, the ionophore A23187 (calcimycin) 4% (*w*/w) was added (uncoupled activity), and the kinetics followed for about 2 min in the absence or in the presence of increasing concentrations of POMs, as described above. After the addition of all the components, the final volume was 1 mL. For each experimental condition, the experiments were always performed in triplicate. Therefore, the determination of Ca^{2+}-ATPase activity without and with the inhibitor was made using a continuous enzymatic method using the measurement of absorbance versus time, as described elsewhere [14,27,39,40].

3. Results and discussion

3.1. Synthesis of $(C_6H_{15}N)_4(C_6H_{16}N)_6(VW_{12}O_{40})_2{\cdot}4H_2O$

The title compound, $(C_6H_{15}N)_4(C_6H_{16}N)_6(VW_{12}O_{40})_2{\cdot}4H_2O$ was synthesized from a mixture of V_2O_5 (Aldrich, 98.8%, 1 mmol) and sodium tungstate dihydrate ($Na_2WO_4{\cdot}2H_2O$, Aldrich, 99.8%, 3 mmol) dissolved in 25 mL of distilled water. Triethylamine ($C_6H_{15}N$, Aldrich, 99.8%, 1 mmol) was then added slowly under stirring. Three drops of hydrochloric acid (HCl, 18%) were added while stirring at 70 °C. The solution gradually turned orange at pH 4, and stirring was continued for 5 h under reflux at 70 °C, resulting in a final pH of 3 (Fig. 1). The reaction mixture was filtered, and the filtrate was allowed to evaporate slowly at room temperature. Orange crystals suitable for single-crystal X-ray diffraction were obtained after approximately 20 days (Fig. 1). All characterization techniques (SC-XRD, Uv–vis spectroscopy, TG analysis, IR spectroscopy, and CHN elemental analysis) confirmed the consistency of the composition and structure. The title compound was obtained in a yield of 1.38 g, corresponding to 20%. CHN elemental analysis of the final compound gave the following results (calculated for $C_{60}H_{164}N_{10}V_2W_{24}O_{84}$, M = 6884.1 g/mol: C = 10.47%, H = 2.40%, *N* = 2.03%; experimental: C = 10.45%, H = 2.38%, *N* = 2.01%), which confirm the presence of the organic component in the hybrid structure.

3.2. Crystallization of the vanadium-substituted Keggin polyoxotungstate

Single crystals of the hybrid compound were obtained by slow evaporation of an aqueous solution of the purified product at room temperature. The reaction mixture was filtered and left to stand at ambient temperature for 20 days, until crystals suitable for single-crystal X-ray diffraction were formed. Selected crystals were mounted under a microscope, and single-crystal X-ray diffraction data were collected at 107 K using a Bruker PHOTON III DUO diffractometer (Bruker AXS GmbH, Karlsruhe, Germany) equipped with a micro-focus sealed X-ray tube.

3.3. Characterization of Keggin-type hybrid

The ORTEP representation of the asymmetric unit of $(C_6H_{15}N)_4(C_6H_{16}N)_6(VW_{12}O_{40})_2{\cdot}4H_2O$ (Fig. 2) clearly displays the Keggin-type polyoxometalate framework, with the trialkylammonium

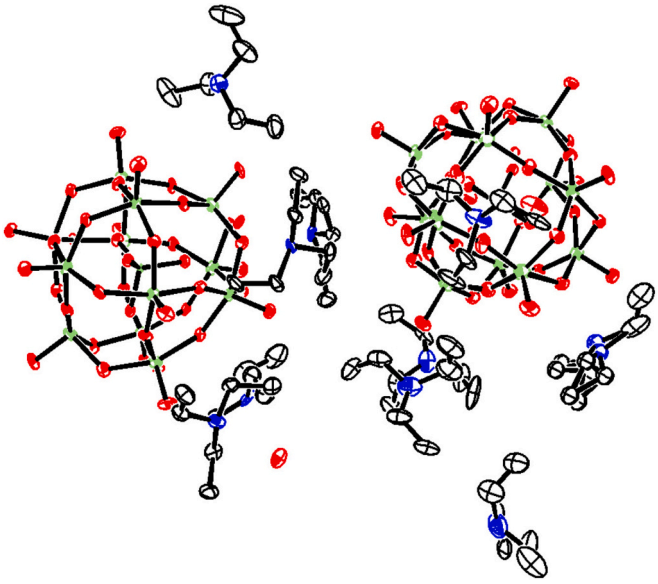

Fig. 2. ORTEP diagram of the asymmetric unit of $(C_6H_{15}N)_4(C_6H_{16}N)_6(VW_{12}O_{40})_2{\cdot}4(H_2O)$.

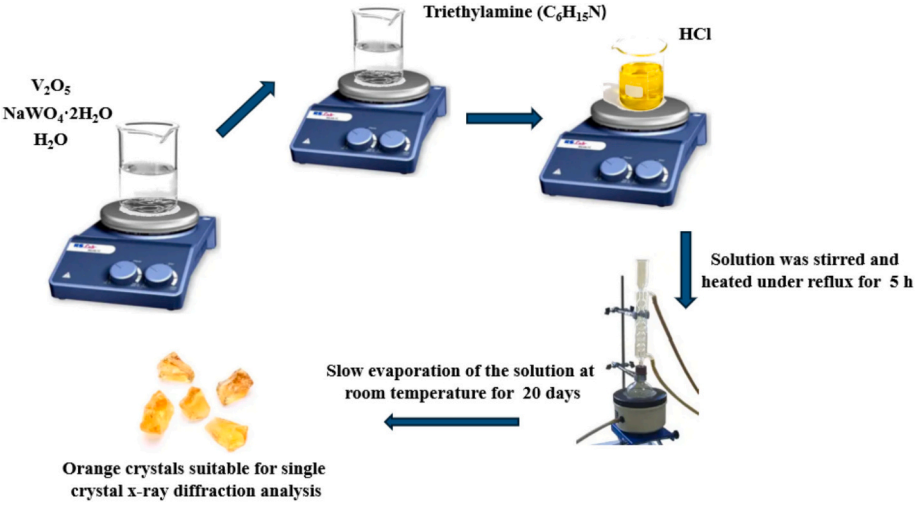

Fig. 1. Schematic representation of the synthesis of $(C_6H_{15}N)_4(C_6H_{16}N)_6(VW_{12}O_{40})_2{\cdot}4H_2O$.

cations arranged around the anion to ensure charge balance. Non-hydrogen atoms are shown as ellipsoids at the 50% probability level, and the figure highlights the spatial orientation of the organic cations and lattice water molecules relative to the POM cluster, thereby confirming the crystal architecture and the interactions stabilizing the solid-state assembly. Single-crystal X-ray diffraction analysis (Table S1) indicates that the compound crystallizes in the triclinic P_1 space group.

Figs. 5 and 6 provide a detailed view of the crystal packing and hydrogen bonding interactions in $(C_6H_{15}N)_4(C_6H_{16}N)_6(VW_{12}O_{40})_2{\cdot}4(H_2O)$ along the [100] and [010] crystallographic directions. The Keggin-type polyanions organize into parallel linear chains along the [100] direction, forming a regular pattern that extends throughout the crystal lattice. Along the [010] direction, the unit cell contains a central polyanion, which is surrounded by four polyanions positioned at the corners of the cell. Organic cations are intercalated between these polyanions, establishing multiple N–H···O hydrogen bonds with terminal oxygen atoms of the polyanions (Table S3). These interactions serve to balance the negative charge of the anionic framework and contribute significantly to the stabilization of the three-dimensional network. The unit cell edges, indicated in the Figs. 3 and 4, clearly show the spatial relationships among polyanions and organic cations molecules, revealing how the combination of linear polyanion chains, intercalated cations, and extensive hydrogen bonding interactions results in a robust and well organized crystalline assembly. This detailed structural organization highlights the crucial role of hydrogen bonding interactions in maintaining the integrity and stability of the crystal lattice.

The thermogravimetric curve of $(C_6H_{15}N)_4(C_6H_{16}N)_6(VW_{12}O_{40})_2{\cdot}4(H_2O)$ shows a multi-step weight loss corresponding to its composition (Fig. 5). The first slight decrease in mass, occurs between 50 and 150 °C and is attributed to the loss of crystallization water molecules. A more significant mass loss is observed between 200 and 500 °C, which can be ascribed to the gradual decomposition of the organic cations, including triethylamine ($C_6H_{15}N$) and trethyllammonium ($C_6H_{16}N$) ions. At temperatures above 600 °C, the remaining residue of the initial mass, is stable and corresponds to the inorganic polyoxometalate framework ($VW_{12}O_{40}$), likely forming metal oxides such as WO_3 and V_2O_5. These observations confirm the presence of lattice water and organic counterions and demonstrate the high thermal stability of the polyoxometalate structure [41].

The infrared spectrum of the Keggin type hybrid $(C_6H_{15}N)_4(C_6H_{16}N)_6(VW_{12}O_{40})_2{\cdot}4(H_2O)$ (Fig. 5B) shows distinct bands corresponding to the different components of the material. The broad bands at 3549 and 3473 cm^{-1}, assigned to O—H stretching vibrations, together with the bands at 1737 and 1615 cm^{-1}, attributed to H–O–H bending, indicate the presence of crystallization water molecules involved in an extensive hydrogen-bonding network. The C—H stretching vibrations of the organic cation $(C_6H_{15}N)^+$ appear at 3029, 2800, and 2713 cm^{-1}. The bending vibrations of CH_2/CH_3 groups are observed at 1472 cm^{-1}, while the CH_3 bending appears at 1365 cm^{-1} [42]. The band at 1217 cm^{-1} is assigned to C—N stretching of the organic cation, with possible contributions from M–O–H vibrations of the cluster. The characteristic vibrations of the polyoxometalate framework are observed at 1029, 878, and 737 cm^{-1}, corresponding to M–O–M stretching, and at 961 cm^{-1}, assigned to terminal M = O stretching. The M–O–M bending vibration is observed at 509 cm^{-1} [43]. Overall, these assignments confirm the structural integrity of the polyoxometalate cluster, the effective encapsulation of the organic cations, and the role of water molecules in stabilizing the structure through hydrogen-bonding interactions (Table 1).

Fig. 6 shows the optical absorption spectrum of the hybrid material, measured in aqueous solution (0.1 mM, pH 5, using a 1.0 cm quartz cuvette, baseline corrected with distilled water as reference) over the wavelength range of 200–900 nm. Four absorption features are observed: two weak bands at approximately 220 and 250 nm, an intense band centered around 292 nm, and a broad absorption extending near 380 nm. These spectral features are characteristic of oxygen-to-metal charge-transfer transitions (O → *V/W*), commonly reported for vanadium-substituted Keggin-type polyoxotungstates containing the structural unit $[VW_{12}O_{40}]^{3-}$ [44–46].

The optical band gap energy was determined using Tauc's method [47], based on the equation $(\alpha h\nu)^{1/n} = A(h\nu - Eg)$, where A is a constant, h is Planck's constant, ν is the photon frequency, and n depends on the nature of the electronic transition. For indirect semiconductors, $n = 2$, while for direct semiconductors, $n = 1/2$. A Tauc plot of $(\alpha h\nu)^2$ versus photon energy ($h\nu$), assuming a direct allowed transition ($n = 1/2$), revealed two distinct optical band gaps. The primary band gap ($Eg_1 \approx 2.49$ eV) corresponds to the fundamental electronic transition from the valence band to the conduction band, indicating the onset of optical absorption. This value reflects the intrinsic electronic structure of the inorganic framework and is characteristic of a wide band gap material. A secondary band gap ($Eg_2 \approx 4.36$ eV) was also identified at higher energy, which may be attributed to additional electronic transitions, such as ligand-to-metal charge transfer, transitions involving deeper valence states, or interband excitations. The presence of both gaps suggests that the compound exhibits insulating behavior, with limited electrical conductivity under ambient conditions.

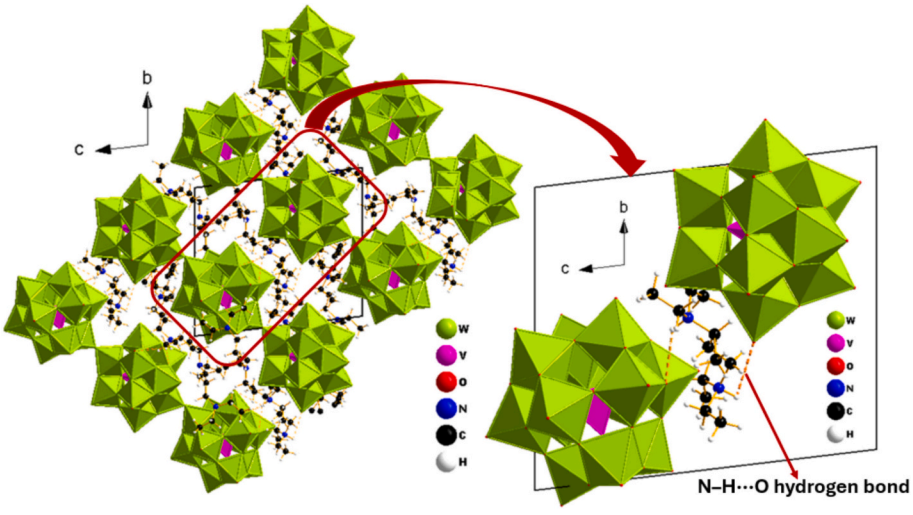

Fig. 3. Hydrogen bonding interactions between the organic cations and terminal oxygen atoms of the polyanions along the [100] direction, with the unit-cell edges shown.

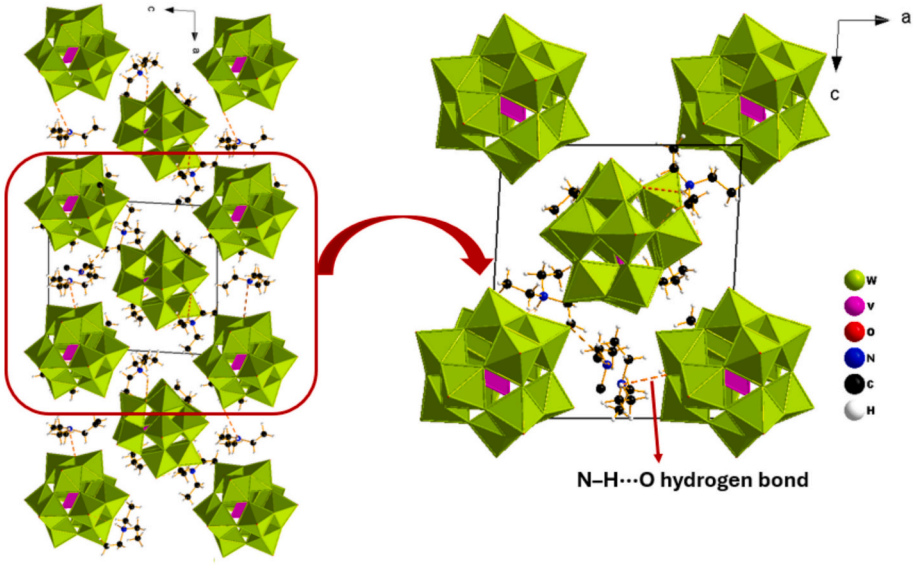

Fig. 4. Hydrogen bonding interactions between the organic cations and terminal oxygen atoms of the polyanions along the [010] direction, with the unit cell edges shown.

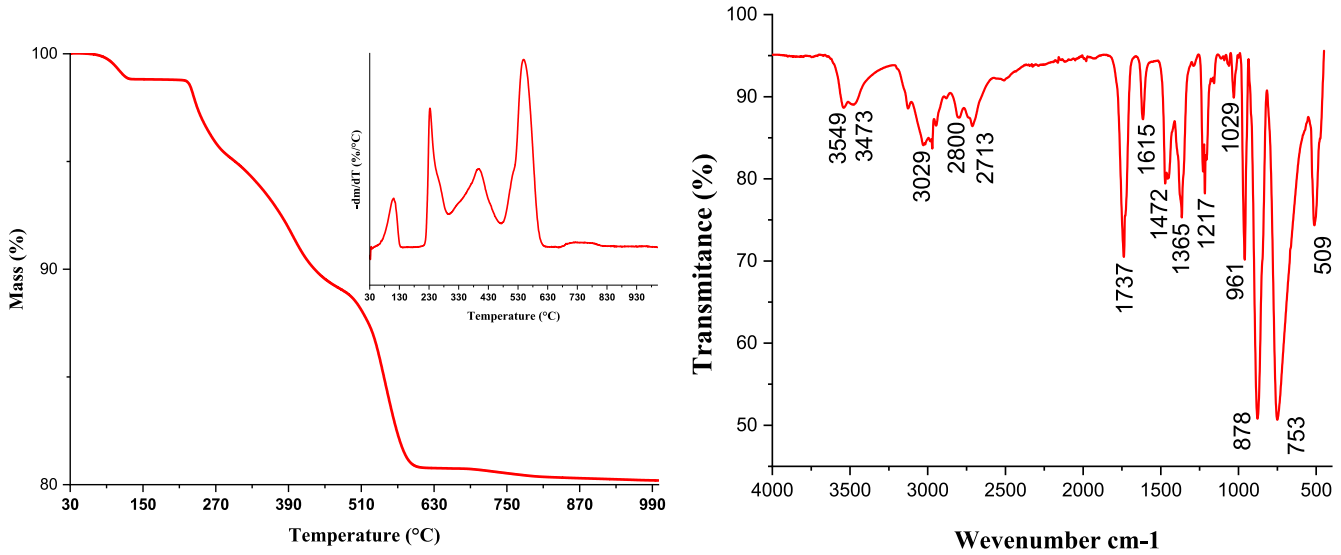

Fig. 5. A) Thermogram of $(C_6H_{15}N)_4(C_6H_{16}N)_6(VW_{12}O_{40})_2{\cdot}4(H_2O)$; B) Infrared spectrum of $(C_6H_{15}N)_4(C_6H_{16}N)_6(VW_{12}O_{40})_2{\cdot}4(H_2O)$.

Table 1
Characteristic infrared absorption bands (cm^{-1}) of the Vanadium-substituted Keggin polyoxotungstate.

Assignment (cm^{-1})	Vibration Symbol
3549	ν(O—H)
3473	ν(O—H)
3029	ν(C—H)
2800	ν(C—H)
2713	ν(C—H)
1737	δ(H–O–H)
1615	δ(H–O–H)
1472	$\delta(CH_2/CH_3)$
1365	$\delta(CH_3)$
1217	ν(C—N) / ν(M–O–H)
1029	ν(M–O–M)
961	ν(M = O)
878	ν(M–O–M)
737	ν(M–O–M)
509	δ(M–O–M)

3.4. Inhibition of Ca^{2+}-ATPase activity by $(C_6H_{15}N)_4(C_6H_{16}N)_6(VW_{12}O_{40})_2{\cdot}4(H_2O)$

The inhibitory potential of the Vanadium-substituted Keggin polyoxotungstate on Ca^{2+}-ATPase activity was evaluated using a coupled pyruvate kinase/lactate dehydrogenase enzyme assay and at the same experimental conditions described before for about 25 POMs [14,27,39,40]. A control assay without inhibitor was included for comparison and for the determination of IC_{50} values. Enzymatic activity was monitored by measuring absorbance as a function of time. The control sample exhibited a higher kinetic slope, indicating maximal ATPase activity, whereas a progressive decrease in the enzymatic kinetic slope was observed with increasing concentrations of the polyoxometalate, as described elsewhere [27]. This reduction in slope reflects the concentration dependent inhibition of Ca^{2+}-ATPase activity by the Vanadium-substituted Keggin polyoxotungstate. Using this method, the effects of the inhibitors can be observed in real time and recorded within 2 to 3 min upon addition of the inhibitor, avoiding putative POMs

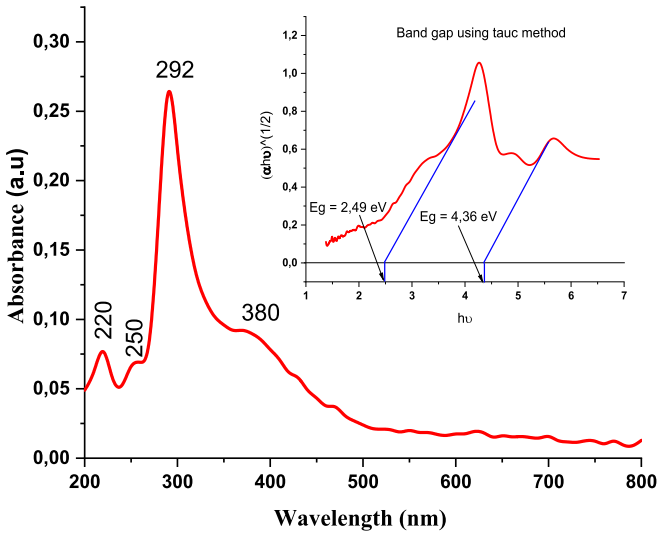

Fig. 6. UV–visible spectrum of $(C_6H_{15}N)_4(C_6H_{16}N)_6(VW_{12}O_{40})_2{\cdot}4(H_2O)$ in aqueous solution, 0.1 mM, pH 5.

decomposition as described previously [14,27,39,40].

POM stability is currently a topic under close attention, as it is essential for understanding the biological effects of POMs. In our studies, direct or indirect experiments are systematically performed to evaluate the stability of POMs under the experimental conditions [14–21]. The POM-1 showed a similar ATPase inhibitory capacity even after 60 min of incubation in the medium under the experimental conditions. As referred above, the ATPase activity inhibition was measured at room temperature only 2–3 min after the addition of POM-1 to the medium. Therefore, we may deduce that the observed ATPase inhibitory activity is attributable to POM-1, as previously described for other POMs using the same experimental model [14,15,27,39,40].

Note that for the experimental conditions used, we do not observe any inhibition of the pyruvate kinase activity using the coupled enzymatic assay. Even for the higher POMs concentrations used, we had always a linear record of the ATPase activity in the presence of the inhibitor, during the 3 min after the POM addition used for the determination of the enzymatic activity, according to previous studies [14,27,39,40]. In the case of any inhibition of the coupled assays enzymes, the ATPase activity cannot be measured in the same mode as observed in the absence of the inhibitor and the ATPase activities in the presence of the several concentrations of the inhibitor cannot be determined. An example of the experimental registration of Ca^{2+}-ATPase inhibition by POMs using the coupled enzymatic assay is shown in the below Fig. S1. In the absence of POM, the control assay displays a higher kinetic slope, whereas increasing concentrations of POM (C1, C2, C3, C4, and C5) lead to progressively lower enzymatic kinetic slopes, reflecting the inhibition of ATPase activity (Fig. S1).

The inhibitory effect of $VW_{12}O_{40}$ on SR Ca^{2+}-ATPase activity was evaluated by plotting the percentage of enzymatic activity as a function of inhibitor concentration. The resulting dose response curve was fitted using an appropriate trendline equation, which was subsequently solved to determine the IC_{50} value, corresponding to 50% inhibition of enzymatic activity. The results obtained for this compound revealed an IC_{50} value of 8.25 μM (Fig. 7).

Using these ATPase vesicles, we have never obtained 100% inhibition with these POMs, as described in previous studies [14,27,39,40]. The Ca^{2+}-ATPase undergoes several conformational states during the Ca^{2+} transport mechanism, such as E1, E1P, E2P, and E2. In addition, it possesses distinct binding sites for Ca^{2+} and ATP, as well as a phosphorylation site at Asp351, which is located far from both the cation and ATP binding sites. Thus, SERCA Ca^{2+}-ATPase exists simultaneously in multiple conformations during its catalytic cycle. This structural and functional complexity explains why we never observed 100% inhibition of the ATPase activity using these POM inhibitors. However, it has been shown that certain POMs, such as decavanadate, display specific affinities for all the different Ca^{2+}-ATPase conformations [40].

Sarcoplasmic reticulum (SR) Ca^{2+}-ATPase vesicles are widely used as an experimental model to investigate the effects of clinically approved drugs on Ca^{2+}-ATPase activity, as well as their impact on calcium transport and homeostasis, with important implications for the treatment of various diseases [15,48,49]. Additionally, Ca^{2+}-ATPase has been identified as a potential target of POMs in cancer, along with other enzymes involved in diverse physiological and pathological processes [11]. Calcium ions (Ca^{2+}) constitute a central intracellular second messenger, orchestrating a wide array of cellular signaling pathways [50]. Accumulating experimental evidence indicates that perturbations in Ca^{2+} homeostasis most notably aberrant increases in cytosolic Ca^{2+} concentrations are critically involved in the pathophysiological cascades underlying neurodegenerative disorders such as Alzheimer's disease [51]. Powered by ATP hydrolysis, these pumps participate in the restoration of resting Ca^{2+} levels following an action potential and in the maintenance of calcium homeostasis [52]. Impairment of these pumps, or pathological Ca^{2+} influx, results in a sustained elevation of

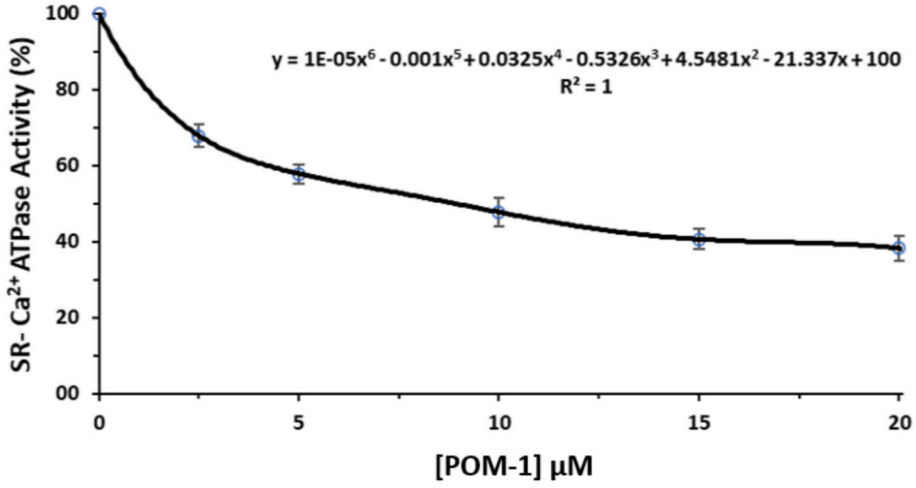

Fig. 7. Inhibition curve of SR- Ca^{2+}-ATPase activity used for the determination of the IC_{50} values of $(C_6H_{15}N)_4(C_6H_{16}N)_6(VW_{12}O_{40})_2{\cdot}4(H_2O)$ (POM-1). Three independent assays were performed for each concentration. IC_{50} value corresponds to inhibitor concentration needed for obtaining 50% of inhibition of control experiment in the absence of the inhibitor.

intracellular calcium levels [53,54]. Such disturbances in calcium homeostasis have severe consequences, triggering a cascade of harmful events, including the activation of cell death–related enzymatic pathways, increased reactive oxygen species (ROS) production, and the induction of inflammatory responses, thereby accelerating the progression of neurodegenerative disorders such as Alzheimer's disease [50].

POMs were shown to inhibit P-type ATPases [14,27,39,40] and to modulate neuronal cytosolic Ca^{2+} concentrations, highlighting their potential as valuable tools for investigating the pathological mechanisms associated with Alzheimer's disease [13,58,59]. More recently, a specific polyoxometalate (P_5W_{30}) have been reported to exhibit agonistic activity toward purinergic P2 receptors in neuronal cells [15], POMs were also identified as the most potent and effective ecto-ATPase inhibitor in cystic fibrosis (CF) airway epithelial cells and referred as putative therapeutic agents to restore hydration of CF airway surfaces [55].

In addition to POMs, several clinically approved compounds including thapsigargin (TG), celecoxib (CE), and cyclopiazonic acid (CPA) are well-established inhibitors of P-type ATPases, notably Ca^{2+}-ATPase. Specifically, TG exhibits IC_{50} values in the range of 0.001–0.029 μM, CPA displays IC_{50} values between 0.1 and 0.2 μM, and CE shows an IC_{50} of approximately 35 μM. Beyond organic molecules, Ca^{2+}-ATPase SR vesicles have also been employed to evaluate the inhibitory capacity of inorganic compounds. Accordingly, several inorganic inhibitors, including polyoxometalates and metal complexes, have been identified as potent Ca^{2+}-ATPase inhibitors, with IC_{50} values spanning from 0.3 to 200 μM comparable to those reported in the present study [14,27,39,40,56–59].

The Keggin-type compound $VW_{12}O_{40}$ (POM-1) investigated in this study demonstrated an IC_{50} of 8.25 μM against Ca^{2+}-ATPase, highlighting its significant inhibitory activity within the context of previously reported polyoxometalates. Compared to the most potent Wells-Dawson derivatives, such as Se_2W_{29} (0.3 μM), P_2W_{15} (0.5 μM), P_2W_{18} (0.6 μM), P_2W_{17} (0.7 μM), and $P_2V_3W_{15}$ (1.0 μM), as well as the Preyssler P_5W_{30} (0.4 μM), $VW_{12}O_{40}$ exhibits moderate potency. Nevertheless, it surpasses the inhibitory activity of several other Keggin-type POMs reported in the literature, including P_2W_{12} (11 μM), SiW_9 (16 μM), MnV_{13} (31 μM), and MnV_{11} (58 μM), demonstrating that it is among the more effective Keggin derivatives. In comparison to smaller or more compact POMs, such as Lindqvist-type $V_2W_4O_{19}$ (45.1 μM) and $V_{2.21}W_{3.79}O_{19}$ (>100 μM), or Anderson-type TeW_6 (200 μM), $VW_{12}O_{40}$ shows a clearly superior inhibitory profile. These data indicate that the classical Keggin architecture of $VW_{12}O_{40}$, combined with its specific metal-oxygen framework, enables substantial interaction with the Ca^{2+}-ATPase active site. Overall, $VW_{12}O_{40}$ serves as an important reference point for Keggin-type POMs, providing a reference point for the design and optimization of novel polyoxometalates targeting Ca^{2+}-ATPase and potentially contributing to strategies aimed at modulating calcium homeostasis in pathological conditions.

3.5. *Hirshfeld surface analysis and Ca^{2+}-ATPase inhibiting potential of hybrid polyoxometalates*

We compare the Ca^{2+}-ATPase inhibition potential of four hybrid polyoxometalates comprising Keggin, Lindqvist, and Dawson frameworks with various organic substituents, which exhibit distinct inhibitory activities against Ca^{2+}-ATPase, namely POM-1 (IC_{50} = 8.25 μM), POM-2 (IC_{50} > > 100 μM), POM-3 (IC_{50} = 3.4 μM), and POM-4 (IC_{50} = 45.1 μM). Moreover, we examine the inhibition potential with their Hirshfeld surface interaction patterns (Table 2). POM-3 (Dawson hybrid: $(C_2H_8N)_6(V_2Mo_{18}O_{62})\cdot 3(H_2O)$) demonstrates the strongest inhibition (IC_{50} = 3.4 μM), which may be linked to the high proportion of polar interactions, particularly H···O and O···O, suggesting electrostatic and hydrogen-bonding contacts with the Ca^{2+}-ATPase. POM-1 (Keggin hybrid: $(C_6H_{15}N)_4(C_6H_{16}N)_6(VW_{12}O_{40})_2\cdot 4(H_2O)$) also shows strong inhibition (IC_{50} = 8.25 μM), reflecting a combination of polar interactions (H···O, H···H) and minor hydrophobic contacts. POM-4 (Lindqvist hybrid: $(C_4H_{16}N_3)_4(V_2W_4O_{19})_3\cdot 12(H_2O)$) shows intermediate inhibition, reflecting a combination of polar interactions (H···O, H···H) and O···O, along with minor hydrophobic interactions. POM-2 (Lindqvist hybrid: $(C_7H_{11}N_2)_4(V_{2.21}W_{3.79}O_{19})\cdot 4(H_2O)$) exhibits weak inhibition (IC_{50}> > 100 μM), largely because of reduced polar interactions and a higher contribution of minor hydrophobic interactions, along with the compact Lindqvist framework potentially limiting enzyme accessibility (Table 2).

The dnorm Hirshfeld surface maps of the four hybrid polyoxometalates (POM-1: Keggin, POM-2: Lindqvist, POM-3: Dawson, POM-4: Lindqvist) were generated (Fig. 8). These maps highlight regions of close intermolecular interactions, where red areas indicate strong contacts, while white and blue regions represent weaker or longer contacts. Among the four POMs, POM-1 and POM-3 show the largest and most intense red regions, indicative of significant H···O and O···O interactions, which are consistent with their low IC_{50} values and high inhibitory activity against Ca^{2+}-ATPase. POM-4 exhibits moderate red areas, reflecting a mixture of polar and minor hydrophobic interactions, in agreement with its intermediate inhibition. In contrast, POM-2 displays only small red regions, indicating fewer polar contacts and more minor hydrophobic interactions, consistent with weak inhibition (IC_{50} > 100 μM). These visualizations provide an overview of how the distribution and type of intermolecular interactions relate to the observed inhibitory potency of each hybrid POM (Fig. 8). However, further studies, such as docking experiments, would be necessary to confirm the interactions between these compounds and the enzyme, and to establish whether hydrogen bonding plays a critical role in their binding strength.

The aim of this analysis was to investigate the relationship between the supramolecular interactions within hybrid polyoxometalates (POMs) and their inhibitory activity against Ca^{2+}-ATPase. Three hybrid POMs were considered: the title compound of this study, POM-1 $[(C_6H_{15}N)_4(C_6H_{16}N)_6(VW_{12}O_{40})_2\cdot 4H_2O]$, and two previously published compounds, POM-2 $[(C_7H_{11}N_2)_4C_2H_8N)_6(V_2Mo_{18}O_{62})\cdot 3H_2O]$ and POM-3 $[(C_4H_{16}N_3)_4(V_2W_4O_{19})_3\cdot 12H_2O]$. Hirshfeld surface analyses were conducted to quantify the percentage of intermolecular contacts, specifically H···O, O···O, and H···H interactions, which are indicative of hydrogen bonding and other non-covalent interactions. Analysis of the three hybrid POMs revealed that only H···O interactions showed a putative correlation with Ca^{2+}-ATPase inhibiting potential, while other contacts such as O···O or H···H did not exhibit significant trend. POM-1 (H···O 59.7%) exhibits strong inhibition (IC_{50} = 8.25 μM), whereas POM-3 (H···O 52%) demonstrates weak activity (IC_{50} > 100 μM), and POM-4 (H···O 68.5%) shows intermediate inhibition (IC_{50} = 45.1 μM).

This selective correlation indicates that classical hydrogen bonds between the POM oxygen atoms and polar residues in the enzyme active site may be key determinants of binding strength, while non-directional interactions such as O···O and H···H appear to play a minor role. These findings suggest the important role of H···O hydrogen bonding in modulating the enzymatic inhibition of Ca^{2+}-ATPase by hybrid POMs, as suggested elsewhere using another biological system [60] (Fig. 9). POM-2 was not included in this analysis because no Ca^{2+}-ATPase inhibition was observed at concentrations up to 100 μM.

Although further studies are undoubtedly required, investigating potential correlations between structural and electronic parameters and functional performance is essential for defining future research directions in the field of polyoxometalates. Over the past five years, studies exploring such correlations, particularly those linking Hirshfeld charges, electrostatic potentials, and DFT-derived descriptors to experimental activity, have been limited in the literature [60–63]. Recent reviews have highlighted the growing interest in polyoxometalates for diverse applications, including ruthenium-containing POMs for catalysis and biomedical uses [64], POMs in electrochemical energy storage [65], and POM-based materials for electron-related devices [66], underscoring the importance of understanding structure–property–function relationships to direct future material design. Reported examples

Table 2
Comparison of intermolecular interactions on the Hirshfeld surface and potential Ca^{2+}-ATPase inhibiting potential of a Keggin hybrid POM with two Lindqvist and one Dawson polyoxometalates.

Hirshfeld Interaction/ Parameter	$(C_6H_{15}N)_4(C_6H_{16}N)_6(VW_{12}O_{40})_2{\cdot}4(H_2O)$, POM-1	$(C_7H_{11}N_2)_4(V_{2.21}W_{3.79}O_{19}){\cdot}4(H_2O)$, POM-2	$(C_2H_8N)_6(V_2Mo_{18}O_{62}){\cdot}3(H_2O)$, POM-3	$(C_4H_{16}N_3)_4(V_2W_4O_{19})_3{\cdot}12(H_2O)$, POM-4
POM Type	Keggin	Lindqvist	Dawson	Lindqvist
H···O (%)	59.7	52	51.8	68.5
O···O (%)	3.3	1.6	27.0	11.6
C···C (%)	0	2.8	0	0
C···H (%)	3.5	6.1	1.5	0
V···O (%)	0	2.7	0	0
W···O (%)	0	1.4	0	0
H···H (%)	32.5	29.7	4.2	19.9
C···O (%)	0.7	0.1	4.3	0
N···H (%)	0	1.5	0.1	0
N···C (%)	0	1.8	0	0
N···O (%)	0.3	0	11.2	0
IC_{50} (μM)	8.25	$>>100$	3.4	45.1
Major Interaction Types	H···O, H···H	H···O, H···H	H···O, O···O	H···O, H···H, O···O
Minor Interaction Types	C···C, V···O, W···O, N···H, N···C	N···O, C···O	C···C, V···O, W···O, N···H, N···C	C···C, C···H, V···O, W···O, C···O, N···H, N···C, N···O
Predicted Activity Trend	Strong inhibition	Weak inhibition	Strong inhibition	Intermediate inhibition
Overall Interpretation	High contributions of H···O and H···H interactions may suggest favorable binding interactions with the enzyme; the Keggin framework could provide a favorable orientation of the organic groups, resulting in an IC_{50} of 8.25 μM	Lower polar interactions and presence of minor hydrophobic contacts may could reduce binding; compact Lindqvist core limits enzyme accessibility; $IC_{50} >> 100$ μM	Strong polar interactions (H···O; O···O) and large Dawson framework could enhance binding; minimal minor interactions; $IC_{50} = 3.4$ μM	Combination of H···O, H···H, and O···O suggests a potential for moderate binding; Lindqvist framework with organic moieties contributes to intermediate inhibition; $IC_{50} = 45.1$ μM

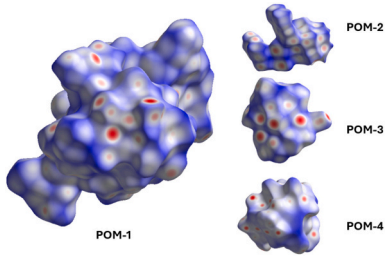

Fig. 8. Combined dnorm Hirshfeld surface maps of the four hybrid polyoxometalates (POM-1, POM-2, POM-3, POM-4) showing differences in intermolecular interaction patterns.

include the correlation between Hirshfeld potential and cytotoxic activity in flavonoid and chromanone derivatives reported by Małecka and co-workers, where variations in molecular geometry and electronic density distribution were demonstrated to modulate intermolecular interactions with biological targets [61.

From a theoretical perspective, Guermi and Saal [63] showed through DFT investigations of Anderson-type polyoxometalates that structural parameters such as metal–oxygen bond lengths, coordination environment, and symmetry govern frontier molecular orbitals, chemical hardness, and thermodynamic stability, thereby controlling intrinsic reactivity [62]. Furthermore, Diaz-Uribe and co-workers [63] reported that modification of TiO_2 thin films with Anderson-type POMs containing Cr, Co, or Ni induces significant electronic band-structure changes, including band-gap narrowing and enhanced charge-transfer efficiency, resulting in improved photocatalytic performance [63]. In a bioinorganic context, Brito and co-workers, demonstrated that a mixed-valence pentadecavanadate exhibits enhanced Ca^{2+}-ATPase inhibition and anti-breast cancer activity, which were directly attributed to electron delocalization and redox flexibility imposed by the POM framework geometry [61]. This high inhibitory activity is also related to the POM's negative surface charge and electrostatic potential, which likely favor binding to positively charged regions of the enzyme, highlighting the role of electrostatic complementarity in protein–POM interactions.

This study highlights distinct differences in intermolecular interaction patterns between a Keggin hybrid polyoxometalate; Lindqvist- and Dawson-type POMs, as revealed by Hirshfeld surface analysis. Variations in hydrogen bonding and oxygen-based contacts suggest that surface interaction features may influence the observed Ca^{2+}-ATPase inhibiting potential.

However, no direct or definitive correlation between intramolecular interactions and Ca^{2+}-ATPase inhibition was established. Enzyme inhibition is governed by factors beyond solid-state interactions, including solution behavior, solvation effects, and the dynamic nature of protein–ligand interactions. Thus, while the analysis suggests potential influence of surface features, further investigation is required to confirm the underlying mechanisms. Future work should combine Hirshfeld surface analysis with computational modeling of POM–enzyme interactions and experimental studies under biological conditions. Expanding the dataset to include structurally related POMs and fine-tuning hybrid architectures will be essential for better understanding and optimizing POM-based Ca^{2+}-ATPase inhibitors.

Thus, POMs, particularly Dawson and Lindqvist types, function as effective inhibitors of Ca^{2+}-ATPase inhibitors by leveraging their high negative charge and strong redox capabilities, with IC_{50} values as low as 8 μM such as VW_{12}. Integrating these POMs into metal organic frameworks (MOFs) allows for enhanced stability, controlled delivery, and potential for enzyme immobilization, sensors, drug delivery, among others applications [67–69].

4. Conclusions

In this work, a Vanadium-substituted Keggin-type polyoxotungstate was successfully synthesized and characterized using a combination of spectroscopic and structural techniques, including X-ray diffraction, UV–visible spectroscopy, infrared spectroscopy and thermogravimetric analysis. These analyses confirmed the preservation of the Keggin framework upon vanadium substitution. Hirshfeld surface analysis provided valuable insights into the nature and contribution of intermolecular interactions governing the solid-state architecture of the compound. Biological evaluation revealed significant Ca^{2+}-ATPase inhibitory activity, a possible relationship between the observed activity and surface interaction features, particularly hydrogen bonding and metal–oxygen contacts identified by Hirshfeld analysis, may be suggested, although no direct correlation can be firmly established from the

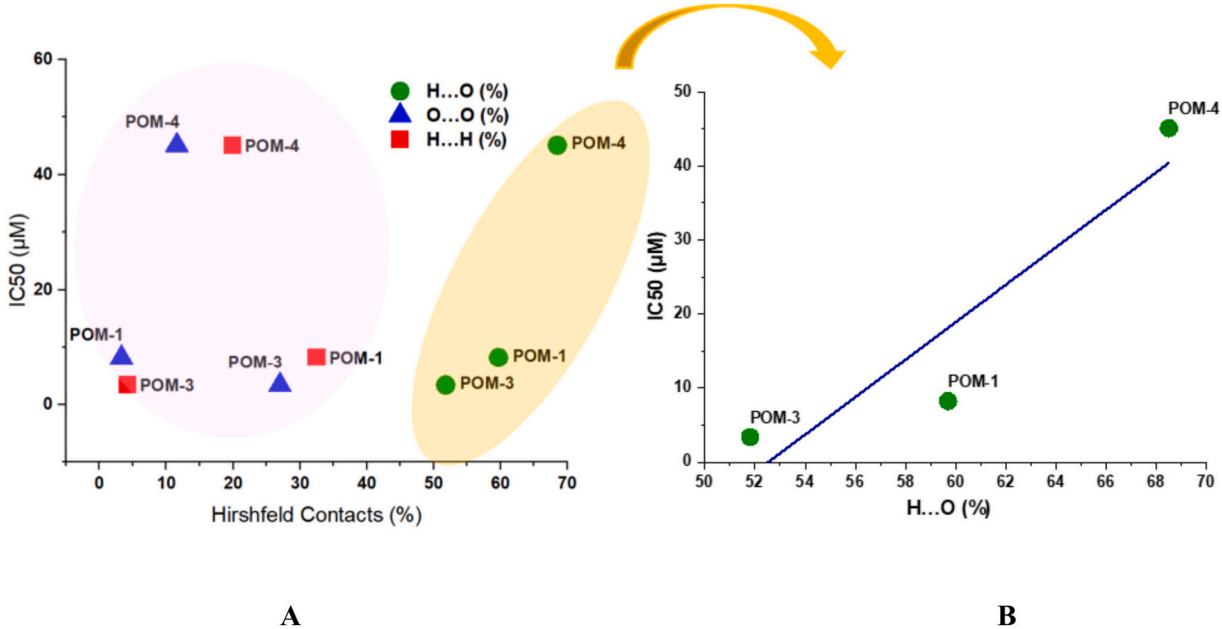

Fig. 9. A) Correlation between Hirshfeld contact percentages (H···O, O···O, H···H) and IC_{50} Ca^{2+}-ATPase inhibition values for 3 hybrid POMs. B) A putative correlation can be found for the percentage of hydrogen-oxygen interactions with the Ca^{2+}-ATPase inhibiting potential.

present data. These findings indicate that intermolecular interactions could contribute to modulating enzymatic inhibition. Overall, this study provides preliminary insight into the relationship between structural features and Ca^{2+}-ATPase inhibition in Vanadium-substituted Keggin polyoxotungstates, rather than a definitive structure–activity relationship. Future investigations will focus on extending this approach to other substituted Keggin systems and combining Hirshfeld analysis with computational and biological studies to better understand their inhibitory mechanisms and potential therapeutic applications.

CRediT authorship contribution statement

Islem Meskini: Writing – original draft, Validation, Methodology, Investigation, Formal analysis, Data curation, Conceptualization. **Gil Fraqueza:** Writing – review & editing, Visualization, Supervision, Methodology, Investigation. **Frédéric Capet:** Writing – review & editing, Validation, Methodology, Investigation, Formal analysis. **Manuel Aureliano:** Writing – review & editing, Writing – original draft, Visualization, Validation, Supervision, Project administration, Methodology, Investigation, Funding acquisition, Formal analysis, Data curation, Conceptualization. **Brahim Ayed:** Writing – review & editing, Writing – original draft, Validation, Supervision, Methodology, Investigation, Formal analysis, Data curation, Conceptualization.

Funding

Thanks to Algarve University, to Erasmus+ International Credit Mobility project funded by the Portuguese National Agency and to Portuguese national funds from FCT - Foundation for Science and Technology, through contracts UID/04326/2025, UID/PRR/04326/2025 and LA/P/0101/2020 (DOI:10.54499/LA/P/0101/2020) and from the operational programmes CRESC Algarve 2020 and COMPETE 2020 through project EMBRC.PT ALG-01-0145-FEDER-022121.

Declaration of competing interest

The authors declare that they have no known competing financial interests or personal relationships that could have appeared to influence the work reported in this paper.

Appendix A. Supplementary data

Supplementary data to this article can be found online at https://doi.org/10.1016/j.jinorgbio.2026.113367.

References

[1] B.C. Ong, H.K. Lim, C.Y. Tay, T.-T. Lim, Z. Dong, Polyoxometalates for bifunctional applications: catalytic dye degradation and anticancer activity, Chemosphere 286 (2022) 131869, https://doi.org/10.1016/j.chemosphere.2021.131869.
[2] S. Wang, X. Geng, Z. Zhao, M. Zhang, Y. Song, K. Sun, Q. Zhang, Ammoniated-driven green synthesis of charged polyoxometalate supported ionic liquids for exceptional heavy metal remediation in actual industrial wastewater, Water Res. 272 (2025) 122939, https://doi.org/10.1016/j.watres.2024.122939.
[3] X. Qiu, R. Wang, Polyoxometalate-based photocatalytic new materials for the treatment of water pollutants: mechanism, advances, and challenges, Catalysts 15 (2025) 613, https://doi.org/10.3390/catal15070613.
[4] Y. Song, T. Bo, J.-C. Ma, J.-F. Ma, Highly efficient photoelectrocatalytic degradation for ciprofloxacin with a new polyoxometalate-based metal–organic hybrid/$BiVO_4$ photoanode, Green Energy Environ. 10 (2025) 1531–1542, https://doi.org/10.1016/j.gee.2025.01.007.
[5] H. Nourolahi, S. Farhadi, R. Malakooti, M. Maleki, F. Mahmoudi, Construction of lacunary α-$K_8SiW_{11}O_{39}$ polyoxometalate/MIL-101(Cr) MOF/$CoFe_2O_4$ magnetic nanocomposites for adsorptive removal of toxic azo dyes and antibiotics from wastewater, CrystEngComm 27 (2025) 1185–1205, https://doi.org/10.1039/D5CE00013K.
[6] I. Gregorovic, N. Lotfian, R. Khajavian, S. Maity, M. Mirzaei, S.S. Mal, M. Aureliano, A. Rompel, Polyoxometalates in environmental remediation, Environ. Sci. Nano 14 (2026) (in press).
[7] A. Bijelic, M. Aureliano, A. Rompel, The antibacterial activity of polyoxometalates: structures, antibiotic effects and future perspectives, Chem. Commun. 54 (2018) 1153–1169, https://doi.org/10.1039/C7CC07549A.
[8] M. Moghadasi, M. Abbasi, M. Mousavi, M. Mirzaei, Polyoxometalate-based materials in therapeutic and biomedical applications: current status and perspective, Dalton Trans. 54 (2025) 6333–6345, https://doi.org/10.1039/D4DT03428G.
[9] M.B. Čolović, D.Z. Krstić, T.D. Lazarević-Pašti, A.M. Bondžić, V.M. Vasić, Polyoxometalates in biomedicine: update and overview, Curr. Med. Chem. 27 (2020) 362–379, https://doi.org/10.2174/0929867327666201207115339.
[10] M.J. Woźniak-Budych, et al., The future of polyoxymetalates for biological and chemical applications, Coord. Chem. Rev. 493 (2023) 215306, https://doi.org/10.1016/j.ccr.2023.215306.
[11] A. Bijelić, M. Aureliano, A. Rompel, Polyoxometalates as potential next-generation metallodrugs in the combat against cancer, Angew. Chem. Int. Ed. 58 (2019) 2980–2999, https://doi.org/10.1002/anie.201803868.
[12] S.I. Gonzalez-Cano, et al., Polyoxidovanadates: a new therapeutic alternative for neurodegenerative and aging diseases, Neural Regen. Res. 19 (2024) 571–577, https://doi.org/10.1234/nrr.2024.123456.
[13] M. Aureliano, J. Mateus, D.M. Rijo, Polyoxometalates' Progress for the treatment of Alzheimer's disease, BioChem 5 (2025) 41, https://doi.org/10.3390/biochem5040041.
[14] M. Aureliano, G. Fraqueza, M. Berrocal, J.J. Córdoba-Granados, N.I. Gumerova, A. Rompel, C. Gutiérrez-Merino, A.M. Mata, Inhibition of SERCA and PMCA Ca^{2+}-ATPase activities by polyoxotungstates, J. Inorg. Biochem. 236 (2022) 111952, https://doi.org/10.1016/j.jinorgbio.2022.111952.
[15] J. Poejo, N.I. Gumerova, A. Rompel, A.M. Mata, M. Aureliano, C. Gutiérrez-Merino, Unveiling the agonistic properties of Preyssler-type polyoxotungstates on purinergic P2 receptors, J. Inorg. Biochem. 259 (2024) 112640, https://doi.org/10.1016/j.jinorgbio.2024.112640.
[16] M. Aureliano, N.I. Gumerova, G. Sciortino, E. Garribba, A. Rompel, D.C. Crans, Polyoxovanadates with emerging biomedical activities, Coord. Chem. Rev. 447 (2021) 214143, https://doi.org/10.1016/j.ccr.2021.214143.
[17] M. Aureliano, N.I. Gumerova, G. Sciortino, E. Garribba, C.C. McLauchlan, A. Rompel, D.C. Crans, Polyoxidovanadates' interactions with proteins: An overview, Coord. Chem. Rev. 454 (2022) 214344, https://doi.org/10.1016/j.ccr.2022.214344.
[18] G. Sciortino, M. Aureliano, E. Garribba, Rationalizing the decavanadate(V) and oxidovanadium(IV) binding to G-actin and the competition with decaniobate(V) and ATP, Inorg. Chem. 60 (2021) 334–344, https://doi.org/10.1021/acs.inorgchem.0c02971.
[19] M. Aureliano, A.L. De Sousa-Coelho, C.C. Dolan, D.A. Roess, D.C. Crans, Biological consequences of vanadium effects on formation of reactive oxygen species and lipid peroxidation, Int. J. Mol. Sci. 24 (2023) 5382, https://doi.org/10.3390/ijms24065382.
[20] A.L. De Sousa-Coelho, G. Fraqueza, M. Aureliano, Repurposing therapeutic drugs complexed to vanadium in Cancer, Pharmaceuticals 17 (2024) 12, https://doi.org/10.3390/ph17010012.
[21] M. Aureliano, The future is bright for polyoxometalates, BioChem 2 (1) (2022) 8–26, https://doi.org/10.3390/biochem2010002.
[22] M.I.S. Veríssimo, D.V. Evtuguin, M.T.S.R. Gomes, Polyoxometalate functionalized sensors: a review, Front. Chem. 10 (2022) 840657, https://doi.org/10.3389/fchem.2022.840657.
[23] R. Liu, C. Streb, Polyoxometalate-single atom catalysts (POM-SACs) in energy research and catalysis, Adv. Energy Mater. 11 (25) (2021) 2101120, https://doi.org/10.1002/aenm.202101120.
[24] J.-H. Kruse, M. Langer, I. Romanenko, I. Trentin, D. Hernández-Castillo, L. González, F.H. Schacher, C. Streb, Polyoxometalate-soft matter composite materials: design strategies, applications, and future directions, Adv. Funct. Mater. 32 (50) (2022) 2208428, https://doi.org/10.1002/adfm.202208428.
[25] A. Gillet, S. Cher, M. Tassé, T. Blon, S. Alves, G. Izzet, B. Chaudret, A. Proust, P. Demont, F. Volatron, S. Tricard, Polarizability is a key parameter for molecular electronics, Nanoscale Horiz. 6 (2021) 271–276, https://doi.org/10.1039/D0NH00583E.
[26] S.A. Hassan, D.M. Aziz, M.N. Abdullah, A.R. Bhat, R.S. Dongre, T.B. Hadda, F. A. Almalki, S.M.A. Kawsar, A.K. Rahiman, S. Ahmed, M.H. Abdellattif, M. Berredjem, S.A. Sheikh, J. Jamalis, In vitro and in vivo evaluation of the antimicrobial, antioxidant, cytotoxic, Hemolytic activities and in silico POM/DFT/DNA-binding and pharmacokinetic analyses of new Sulfonamide bearing Thiazolidin-4-ones, J. Biomol. Struct. Dyn. 42 (2024) 3747–3763, https://doi.org/10.1080/07391102.2023.2226713.
[27] I. Meskini, F. Capet, G. Fraqueza, N. Dege, M.N. Tahir, B. Ayed, M. Aureliano, Dawson- and Lindqvist-type hybrid polyoxometalates: synthesis, characterization and Ca^{2+}-ATPase inhibition potential, Molecules 30 (22) (2025) 4334, https://doi.org/10.3390/molecules30224334.
[28] A. Satya, A. Bhattacharjee, Proposed biosensor for the detection of bovine serum albumin using 7CB liquid crystals: a preliminary study, Int. J. Biol. Macromol. 289 (2025) 138881, https://doi.org/10.1016/j.ijbiomac.2024.138881.
[29] S. Lentink, D.E. Salazar Marcano, M.A. Moussawi, T.N. Parac-Vogt, Exploiting interactions between polyoxometalates and proteins for applications in (bio) chemistry and medicine, Angew. Chem. Int. Ed. 62 (2023) e202303817, https://doi.org/10.1002/anie.202303817.
[30] Y. Zeng, P. Qi, Y. Wang, C. Chen, D. Zhang, DNA pom-pom nanostructure as a multifunctional platform for pathogenic Bacteria determination and inactivation, Biosens. Bioelectron. 177 (2021) 112982, https://doi.org/10.1016/j.bios.2021.112982.
[31] I.F. Gette, I.G. Danilova, M.O. Tonkushina, A.A. Ostroushko, The impact of iron–molybdenum polyoxometalates and a mixture of nanoparticle components on the content of nucleic acids and histone proteins in rat blood lymphocytes,

Nanotechnol. Russia 15 (2020) 191–197, https://doi.org/10.1134/S1995078020020081.
[32] N. Gao, Z. Liu, H. Zhang, C. Liu, D. Yu, J. Ren, X. Qu, Site-directed chemical modification of amyloid by polyoxometalates for inhibition of protein misfolding and aggregation, Angew. Chem. Int. Ed. 61 (2022) e202115336, https://doi.org/10.1002/anie.202115336.
[33] D.E. Salazar Marcano, J.-J. Chen, M.A. Moussawi, G. Kalandia, A.V. Anyushin, T. N. Parac-Vogt, Redox-active polyoxovanadates as cofactors in the development of functional protein assemblies, J. Inorg. Biochem. 260 (2024) 112687, https://doi.org/10.1016/j.jinorgbio.2024.112687.
[34] M.A. Spackman, D. Jayatilaka, Hirshfeld surface analysis, CrystEngComm 11 (2009) 19–32, https://doi.org/10.1039/B818330A.
[35] V. Psycharis, D. Dermitzaki, C.P. Raptopoulou, The use of Hirshfeld surface analysis tools to study the intermolecular interactions in single molecule magnets, Crystals 11 (10) (2021) 1246, https://doi.org/10.3390/cryst11101246.
[36] A. Maalaoui, O. Pérez, M. Rzaigui, S. Toumi Akriche, Enhancement with Hirshfeld surface analysis of structural, electrical, dielectric and luminescent performance of two bioactive V-substituted polytungstates, J. Alloys Compd. (2017), https://doi.org/10.1016/j.jallcom.2016.10.231.
[37] G.M. Sheldrick, A short history of SHELX, Acta Crystallogr. A 64 (2008) 112–122, https://doi.org/10.1107/S0108767307043014.
[38] G.M. Sheldrick, Crystal structure refinement with SHELXL, Acta Crystallogr. C 71 (2015) 3–8, https://doi.org/10.1107/S2053229614027420.
[39] N.I. Gumerova, L. Krivosudský, G. Fraqueza, J. Breibeck, E. Al Sayed, E. Tanuhadi, A. Bijelić, J. Fuentes Moreno, M. Aureliano, A. Rompel, The P-type ATPase inhibiting potential of polyoxotungstates, Metallomics 10 (2018) 287–295, https://doi.org/10.1039/C7MT00369A.
[40] G. Fraqueza, C.A. Ohlin, W.H. Casey, M. Aureliano, Sarcoplasmic reticulum calcium ATPase interactions with decaniobate, decavanadate, vanadate, tungstate, and molybdate, J. Inorg. Biochem. 107 (2012) 82–89, https://doi.org/10.1016/j.jinorgbio.2011.11.010.
[41] M.-X. Yang, S. Lin, X.-H. Chen, M.-H. Luo, J.-H. Liu, Two organic–inorganic hybrid compounds constructed from 12-tungstovanadate and bipyridine, J. Coord. Chem. 62 (2009) 406–417, https://doi.org/10.1080/00958970903431704.
[42] C.A. Téllez, E. Hollauer, M.A. Mondragón, V.M. Castaño, Fourier transform infrared and Raman spectra, vibrational assignment and ab initio calculations of terephthalic acid and related compounds, Spectrochim. Acta A Mol. Biomol. Spectrosc. 57 (2001) 667–679, https://doi.org/10.1016/S1386-1425(00)00381-7.
[43] H.-T. Zhu, Y. Sun, F. Su, Y.-J. Zhang, X.-J. Sang, J. Ren, L.-C. Zhang, Self-assembly of a unique triangle-like tungstovanadate containing pentagonal $\{(WO_7)W_3(SnR)_2\}$ cluster, Dalton Trans. 53 (2024) 10226–10234, https://doi.org/10.1039/D4DT01281J.
[44] Y. Lu, Y. Chin Feng, A potassium-lithium double salt of decavanadate showing unprecedented (6,8)-connected topology, J. Chem. 28 (2010) 2404–2410, https://doi.org/10.1002/cjoc.201190012.
[45] J. Xiong, Y. Niu, H. Xu, G. Cao, B. Liu, H. Hu, G. Xue, Charge-transfer salts based on Lindqvist and Keggin polyoxoanion acceptors and ferrocenyl cationic donors, New J. Chem. 36 (2012) 1234–1240, https://doi.org/10.1039/C2NJ20911J.
[46] S.R. Yerra, S.K. Amanchi, S. Das, Synthesis and structural characterization of Lindqvist-type mixed-metal cluster anion $[V_2W_4O_{19}]^{4-}$ in discrete and coordination polymer compounds, J. Mol. Struct. 1065–1066 (2014) 80–86, https://doi.org/10.1016/j.molstruc.2014.01.005.
[47] P. Peverga, R. Jubu, E. Danladi, U.I. Ndeze, O.O. Adedokun, Comment about the use of unconventional Tauc plots for bandgap energy determination of semiconductors using UV–Vis spectroscopy, Res. Opt. 7 (2024) 100606, https://doi.org/10.1016/j.rio.2024.100606.
[48] F. Tadini-Buoninsegni, S. Smeazzetto, M.R. Moncelli, Drug interactions with the Ca^{2+}-ATPase from sarco(endo)plasmic reticulum (SERCA), Front. Mol. Biosci. 5 (2018) 36, https://doi.org/10.3389/fmolb.2018.00036.
[49] T. Bian, J.M. Autry, D. Casemore, J. Li, D.D. Thomas, Direct detection of SERCA calcium transport and small-molecule inhibition in giant unilamellar vesicles, Biochem. Biophys. Res. Commun. 481 (2016) 206–212, https://doi.org/10.1016/j.bbrc.2016.10.096.
[50] M. Brini, T. Calì, D. Ottolini, E. Carafoli, Neuronal calcium Signaling: function and dysfunction, Cell. Mol. Life Sci. 71 (2014) 2787–2814, https://doi.org/10.1007/s00018-013-1550-7.
[51] M. Joshi, S. Joshi, M. Khambete, M. Degani, Role of calcium dysregulation in Alzheimer's disease and its therapeutic implications, Chem. Biol. Drug Des. 101 (2023) 453–468, https://doi.org/10.1111/cbdd.14175.
[52] T. Boczek, M. Sobolczyk, J. Mackiewicz, M. Lisek, B. Ferenc, F. Guo, L. Zylinska, Crosstalk among calcium ATPases: PMCA, SERCA, and SPCA in mental diseases, Int. J. Mol. Sci. 22 (2021) 2785, https://doi.org/10.3390/ijms22052785.
[53] A.M. Mata, M. Berrocal, D. Marcos, M.R. Sepúlveda, Impairment of PMCA activity by amyloid β-peptide in membranes from Alzheimer's disease-affected brain and from other model systems, Biophys. J. 98 (2010) 170, https://doi.org/10.1016/j.bpj.2009.12.916.
[54] A. Drews, J. Flint, N. Shivji, P. Jönsson, D. Wirthensohn, E. De Genst, C. Vincke, S. Muyldermans, C. Dobson, D. Klenerman, Individual aggregates of amyloid Beta induce temporary calcium influx through the cell membrane of neuronal cells, Sci. Rep. 6 (2016) 31910, https://doi.org/10.1038/srep31910.
[55] C. Van Heusden, B. Button, W.H. Anderson, et al., Inhibition of ATP hydrolysis restores airway surface liquid production in cystic fibrosis airway epithelia, Am. J. Phys. Lung Cell. Mol. Phys. 318 (2020) L356–L365, https://doi.org/10.1152/ajplung.00449.2019.
[56] D. Marques-da-Silva, G. Fraqueza, R. Lagoa, A.A. Vannathan, S.S. Mal, M. Aureliano, Polyoxovanadate inhibition of *Escherichia coli* growth shows a reverse correlation with Ca^{2+}-ATPase inhibition, New J. Chem. 48 (2019) 15016–15027, https://doi.org/10.1039/C9NJ01208G.
[57] A.L. De Sousa-Coelho, M. Aureliano, G. Fraqueza, G. Serrão, J. Gonçalves, I. Sánchez-Lombardo, W. Link, B.I. Ferreira, Decavanadate and metformin-decavanadate effects in human melanoma cells, J. Inorg. Biochem. 235 (2022) 111915, https://doi.org/10.1016/j.jinorgbio.2022.111915.
[58] C. Fonseca, G. Fraqueza, S.A.C. Carabineiro, M. Aureliano, The Ca^{2+}-ATPase inhibition potential of gold(I, III) compounds, Inorganics 8 (2020) 49, https://doi.org/10.3390/inorganics8020049.
[59] G. Fraqueza, J. Fuentes, L. Krivosudský, S. Dutta, S.S. Mal, A. Roller, G. Giester, A. Rompel, M. Aureliano, Inhibition of Na^+/K^+- and Ca^{2+}-ATPase activities by phosphotetradecavanadate, J. Inorg. Biochem. 197 (2019) 110700, https://doi.org/10.1016/j.jinorgbio.2019.110700.
[60] M. Małecka, J. Kusz, L. Eriksson, A. Adamus-Grabicka, E. Budzisz, The relationship between Hirshfeld potential and cytotoxic activity: a study along a series of flavonoid and chromanone derivatives, Molecules 25 (2020) 3680, https://doi.org/10.1107/S205322962000813X.
[61] B.R. Brito, H.S. Camilo, A.F. da Cruz, R.R. Ribeiro, E.L. de Sá, C.C. de Oliveira, G. Fraqueza, G. Klassen, M. Aureliano, G.G. Nunes, Mixed-valence Pentadecavanadate with Ca^{2+}-ATPase inhibition potential and anti-breast Cancer activity, Inorganics 13 (2025) 306, https://doi.org/10.3390/inorganics13090306.
[62] I.N.E.H. Guermi, A. Saal, Theoretical investigation of structural parameters, reactivity behavior, and thermodynamic properties of Anderson polyoxometalate (POM), Int. J. Mol. Sci. 23 (2022) 1231–1240, https://doi.org/10.1007/s11224-022-02088-7.
[63] C. Diaz-Uribe, F. Duran, W. Vallejo, E. Puello, X. Zarate, E. Schott, Photocatalytic study of TiO_2 thin films modified with Anderson-type polyoxometalates (Cr, Co and Ni) : experimental and DFT study, Polyhedron 231 (2023) 116253, https://doi.org/10.1016/j.poly.2022.116253.
[64] Q. Cai, R. Gao, Y. Wang, J. Xing, Q. Zhang, M. Zhu, X. Qin, M. Liao, Y. Huang, Ruthenium containing polyoxometalates: from synthesis, structures, properties to functional applications, J. Inorg. Biochem. 4 (2025) 9140083, https://doi.org/10.26599/POM.2024.9140083.
[65] W. Bao, C. Feng, C. Wang, D. Liu, X. Fan, P. Liang, Polyoxometalates in electrochemical energy storage: recent advances and perspectives, Int. J. Mol. Sci. 26 (21) (2025) 10267, https://doi.org/10.3390/ijms262110267.
[66] Y. Hu, Y. Wang, J. Zhao, L. Chen, Recent advances of polyoxometalate-based materials applied for electron-related devices, Coord. Chem. Rev. 506 (2024) 215724, https://doi.org/10.1016/j.ccr.2024.215724.
[67] A. Alamro, T. Balbaied, Metal–organic frameworks for enzyme modulation in protein kinase and phosphatase regulation—mechanisms and biomedical applications, Kinases & Phosphatases 3 (2025) 21, https://doi.org/10.3390/kinasesphosphatases3040021.
[68] Q. An, Z. Xu, W. Shang, Y. Wang, X. Liu, D. Guo, M. Zeng, Z. Jia, Polyoxometalate-based metal–organic frameworks as the solid support to immobilize MP-11 enzyme for enhancing thermal and recyclable stability, ACS Appl. Bio Mater. 5 (2022) 1222–1229, https://doi.org/10.1021/acsabm.1c01252.
[69] P. Kush, R. Singh, P. Kumar, Recent Advances in Metal–Organic Framework-Based Anticancer Hydrogels, Gels 11 (1) (2025) 76, https://doi.org/10.3390/gels110100.